Rodriguez Padilla, A.M., et al., 2022, Joint earthquake ruptures of the San Andreas and San Jacinto faults, California, USA: Geology, https://doi.org/10.1130/G49415.1

SUPPLEMENTAL MATERIAL

METHODS

Rupture conditions for LCRF triggering

The LCRF is a low-angle, shallow normal fault, located between the SAF and SJF, that by itself is too shallow (Supplemental Figure 1) and too short to be seismogenic or act directly to transfer slip between these faults. Thus, slip on the LCRF is most likely a quasistatic response to slip on these faults or to strong shaking. Normal motion on the LCRF requires strong dilation that overcomes the regional north-south contraction of the Transverse Ranges (Yang and Hauksson, 2013). Strong dilation is expected adjacent to a right-lateral fault rupture, on either or both the SAF and the SJF, that terminates within Cajon Pass.

To test the imposed stress and the optimal slip direction of the LCRF in response to rupture on either or both of the SAF and SJF, we build a suite of Coulomb stress models (Supplemental Figure 2)(Toda et al., 2011). In the models, slip on the neighboring part of the SAF or SJF is tapered to simulate a stress drop of approximately 6 MPa. Based on our Coulomb models, the conditions necessary for dominantly normal slip occur in the presence of right-lateral slip that tapers northward on the SJF (Supplemental Figure 2, middle and right). A scenario involving tapered slip on both the SAF and the SJF (Supplemental Figure 2, right) triggers double the stress change on the LCRF than the scenario involving the SJF alone (Supplemental Figure 2, middle). Rupture that terminates on the SAF without stepping over induces a stronger component of left-lateral slip than normal slip on the LCRF, inconsistent with our field observations.

To further distinguish between our two favorable Coulomb stress models, we built a finite element mesh in Trelis (Supplemental Figure 5) based on the mesh in Lozos et al. (2016). The details of the mesh and inclusion of the LCRF are given in the finite element modeling section of this appendix. Extending the slip distributions used in our Coulomb stress models to more realistic, non-planar faults, we allow the LCRF to slip in response to rupture of the SAF and the SJF. The summary of these models and our Coulomb stress models are in Figure 1 of the main manuscript. Modeled slip on the SJF only imposes 1mm of normal slip on the LCRF (Figure 1, bottom middle), which would not be distinguishable from our paleoseismic record. While different slip conditions (larger slip, steeper slip tapers) on the SJF would trigger larger slip on the LCRF, an increase of over two orders of magnitude would be required to match the >50cm of slip recorded per event in our trench.

Slip on both the SJF and the SAF imposes 10 cm of normal slip on the LCRF (Figure 1, bottom left). The slip per event observed in the trench (50cm-1m) exceeds this number by at least a

factor of 5. This mismatch would be overcome by larger slip on the SJF and the SAF, or steeper slip tapers on these faults. Our models for the 1812 event show such a case (see main manuscript and finite element models section). Thus, while the LCRF may preserve a record of slip on the northern SJF alone, the large slip events described in this manuscript are most likely the product of co-rupture of the SAF and SJF. While we cannot rule out the possibility of lingering Coulomb stresses from ruptures promoting rupture on the adjacent fault, large slip on the LCRF requires steep slip tapers, which are a feature of linked earthquake rupture (Elliott, Dolan, and Oglesby, 2009; Scholz and Lawler, 2004) favoring co-rupture as the main mechanism driving the large slip we observe in the trench.

Trenching

The excavation site for the trench was chosen based on the availability of ponded sediment that would record fault slip. Because the LCRF scarp ruptures through a ridge, depocenters are scarce. A team excavated a 15m long, 1.5m wide, ~ 2-3m deep trench where the uphill-facing fault scarp dams a small, ephemeral channel draining the crest of Lytle Creek Ridge (Figure 1). The strata in the trench were numbered by age, increasing downward. The numbering scheme was developed as trenching proceeded, with gaps between numbers left to accommodate units not yet characterized or subdivided. The trench interpretation is shown in Figure 2. We only show the westernmost 5 meters of the trench, because the remaining 10 meters were not faulted.

Radiocarbon dating

We collected charcoal samples to constrain the age of the stratigraphic units and earthquake event horizons. We collected over 120 samples spanning the entire stratigraphic sequence of the trench. Collection of multiple samples per unit is essential because age determination using detrital charcoal is limited by the effects of inheritance during growth and transport of burned vegetation to the depocenter. We selected and prepared 40 samples in the Keck Center for Accelerator Mass Spectrometry (KeckCAMS) Laboratory at the University of California, Irvine following the standard pre-treatment, combustion, and graphite reduction processes. The selected samples were then measured by the KeckCAMS, and calibrated to calendar years with the Intcal13 radiocarbon calibration curve (Ramsey, 2009; Reimer et al., 2013). We then used OxCal v.4.2., a software for Bayesian analysis of geochronology data, to re-calibrate the probability distribution functions of sample ages to account for stratigraphic ordering (Lienkaemper and Ramsey, 2009) and construct a depth profile of units that then could be used to interpret the timing of events in the trench. Because samples from different layers overlap in age and reversals are common, only the youngest age per unit was included in the Oxcal model. Pollen analysis is required to refine stratigraphic ages younger than ~1650A.D., because of non-unique calibration of 14C dates during this time. We collected pollen samples from every fine-grained unit in the

stratigraphic sequence to obtain additional dating constraints. Pollen analysis bypasses the inheritance problem in the radiocarbon ages but only extends back to the early 1600s.

Invasive pollen species analysis

We collected nine samples from the trench for palynological analysis (Figure 2) from the uppermost strata of the trench. All samples were soil-like sediments, presumably a mixture of aeolian sand, colluvial material, and an organic fraction, mostly fine woody dust, micro-charcoals, phytoliths, and pollen.

To determine the pollen concentration per sample, two Lycopodium tablets (BATCH N177745) were added to each sample (15 g) before the beginning of treatment. We used the standard Faegri-Iversen potassium hydroxide, hydrochloric acid, and acetolysis method for extracting pollen from a mixture of sand, silt, and clay, but with some necessary additions. After the dissolution of carbonates and silicates, the remaining fraction was filtered several times to remove particles coarser than 70 microns, and those finer than 7 microns. From the remaining purified sediment, pollen was extracted using a sodium polytungstate heavy liquid flotation method. The slides are prepared using glycerin and sealed with a varnish.

The objective of our palynological analysis was to identify pollen species non-native to California and to find the possible first appearance of the introduced species. This method was successfully used in the past for dating seismic events in California (e.g. Fumal et al., 2002). Historical records suggest that invasive plant species emerged in California generally in the 18th century (Mensing and Byrne, 1998). We compiled a list of all existing plant species in the Cajon Pass area based on references of plant atlas Calflora (Calflora, 2020). We selected a group of non-native plants from the general list, including 63 different plant genera and a total of 123 species (Supplement Table 1). We then assembled an atlas of pollen images of each invasive species and used it for pollen identification. From 450 to 2050 pollen grains (both introduced and native) were counted for each sample, except for two bottom-most samples (P100 A and P130A) which did not have statistically sufficient pollen. Twenty-seven different invasive species were identified. The absolute and relative amounts of each species of pollen are presented in supplemental Table 1 with the date of their introduction to California. A kite diagram (Figure S4) represents frequencies of occurrence of introduced species along a time transect.

We use the year of introduction of the invasive pollen species present in our samples as constraints in our Bayesian models. Aerial pollen transport occurs at a rate of ~2-20km/yr (Pysek and Humle, 2005). The trenching site is downwind from the two nearest missions, and ~100km away from Los Angeles. To account for the transportation delay in our Oxcal model, we treat our pollen constraints as uniform probability density functions that start at the year of introduction of

the species and extending for 20 years, resulting in a right-triangle truncation of the event PDF (see the example for pollen sample 1 below). We choose 20 years as a conservative range based on the transportation rate range of Pysek and Humle (2005).

Finite element modeling

Because the LCRF is too short and shallow to be seismogenic, large slip events on the LCRF must be driven by strains imposed by rupture events on the San Andreas or San Jacinto faults. Using mechanical modeling, we can use the magnitude of LCRF slip to constrain these strains, and thus the amount and gradient of slip on the northern San Jacinto in these events. We focus on the 1857 event versus the 1812 event given the pre-existing slip distributions available. This process is described in the main body of this manuscript.

We mesh the San Andreas and San Jacinto faults based on the USGS Quaternary Faults Database surface traces with simplified geometries at depth (Lozos, 2016, Supplemental figure 5) using the commercial finite element meshing software Trelis. We use the San Bernardino and Claremont strands of the San Andreas and the San Jacinto respectively (Lozos, 2016). The faults are embedded in a homogeneous, elastic crustal volume 16 km deep, following the work of Lozos (2016). Because the LCRF is most likely aseismic unless it is being driven by the San Andreas and/or the San Jacinto, there is no microseismicity that can aid in mapping its subsurface geometry. Based on its outcrop pattern and dip in the trench, we interpret the LCRF intersects the rough topography of the Lytle Creek Ridge at a shallow angle, resulting in a complex surface trace that is unlikely to be representative of the subsurface geometry. To avoid unrealistic complexity, we mesh the LCRF as a planar, low angle normal fault using the westerly strike and 30° dip measured in the field at six different locations.

Our models assume there are no residual stresses in the LCRF from prior events or tectonic loading that would facilitate triggering from the imposed displacements on the San Andreas and San Jacinto. We use finite element code Pylith (Aagard et al., 2013) to impose kinematic slip on the San Andreas and the San Jacinto faults. The parameters used in the simulations are listed in Supplemental Table 3. In these quasistatic models, the LCRF slips when the static value of friction is overcome and the fault is assumed to be cohesionless. The LCRF ruptures through a range of materials present at different sections of the Pelona Schist, including through bands of serpentine and tonalitic intrusions. We tested a range of friction values to determine the sensitivity of slip on the LCRF to this parameter and found negligible differences within the range of μ = 0.2-0.6. For the final models, we assumed a coefficient of static friction of 0.4.

Supplemental References

Bronk Ramsey, C., 2009, Bayesian analysis of radiocarbon dates: 233 Radiocarbon, v. 51, p. 337–360, https://doi.org/10.1017/S0033822200033865.

Calflora, 2021, Information on California 235 plants for education, research and conservation: Berkeley, California, The Calflora 236 Database, https://www.calflora.org/ (accessed 10 August 2019).

Lienkaemper, J.J., 256 and Bronk Ramsey, C., 2009, OxCal: Versatile tool for developing paleoearthquake 257 chronologies—A primer: Seismological Research Letters, v. 80, p. 431–434, 258 https://doi.org/10.1785/gssrl.80.3.431.

Mensing, S., and Byrne, R., 1998, 275 Pre-mission invasion of *Erodium cicutarium* in California: Journal of Biogeography, 276 v. 25, p. 757–762, https://doi.org/10.1046/j.1365-2699.1998.2540757.x.

Pyšek, P., and Hulme, P.E., 2005, 287 Spatio-temporal dynamics of plant invasions: Linking pattern to process: Écoscience, 288 v. 12, p. 302–315, https://doi.org/10.2980/i1195-6860-12-3-302.1.

Reimer, P.J., et al., 2013, IntCal13 and 290 Marine13 radiocarbon age calibration curves 0–50,000 years cal BP: Radiocarbon, 291 v. 55, p. 1869–1887, https://doi.org/10.2458/azu_js_rc.55.16947.

SUPPLEMENTAL INFORMATION

Frequent Joint Earthquake Rupture of the San Andreas and San Jacinto Faults

Alba M. Rodriguez Padilla[1*], Michael E. Oskin[1], Thomas K. Rockwell[2], Irina Delusina[1], Drake M. Singleton[3].

This PDF file includes:

Supplemental Figures S1 to S7
Supplemental Tables S1 to S3

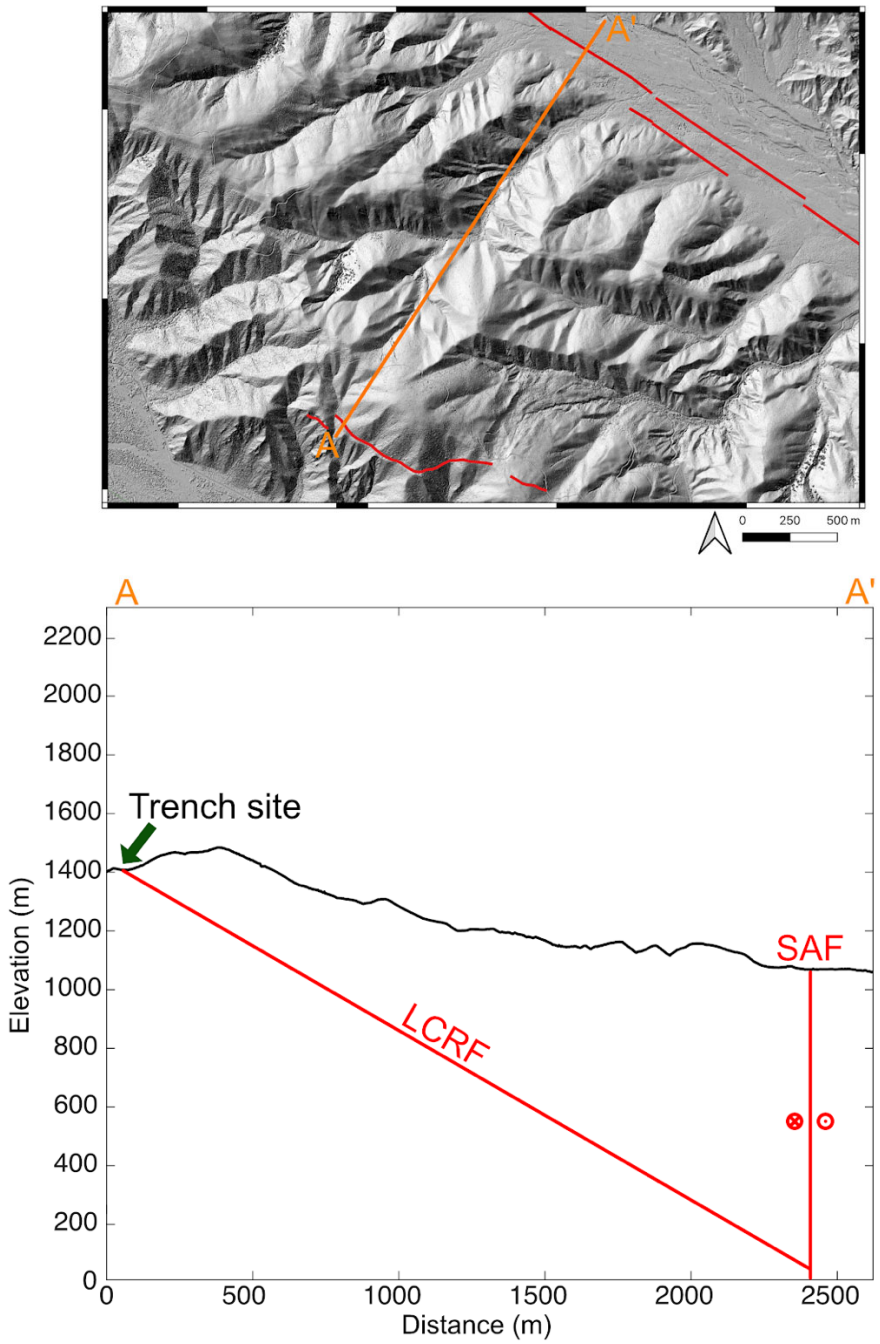

Fig. S1.

Cross-section of the Lytle Creek Ridge Fault (LCRF) based on measurements of strike and dip collected in the field. The LCRF roots into the San Andreas Fault at a shallow depth.

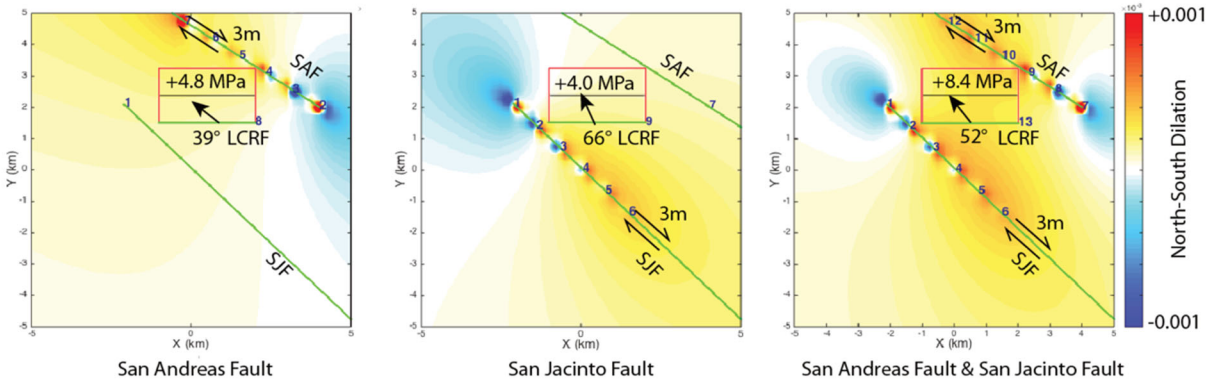

Fig. S2. Coulomb models (Toda et al., 2011) for stress increase and optimal slip direction on a 30° north-dipping LCRF in response to rupture on the vertical San Andreas fault (left), San Jacinto fault (middle), or both (right). Color corresponds to change in north-south dilational strain. In each case, slip is tapered to simulate constant stress drop of approximately 6 MPa, driving a comparable stress increase on LCRF. Highest stress change, with slip direction consistent with that observed in outcrop, occurs for the case where slip occurs on the San Andreas fault and San Jacinto fault.

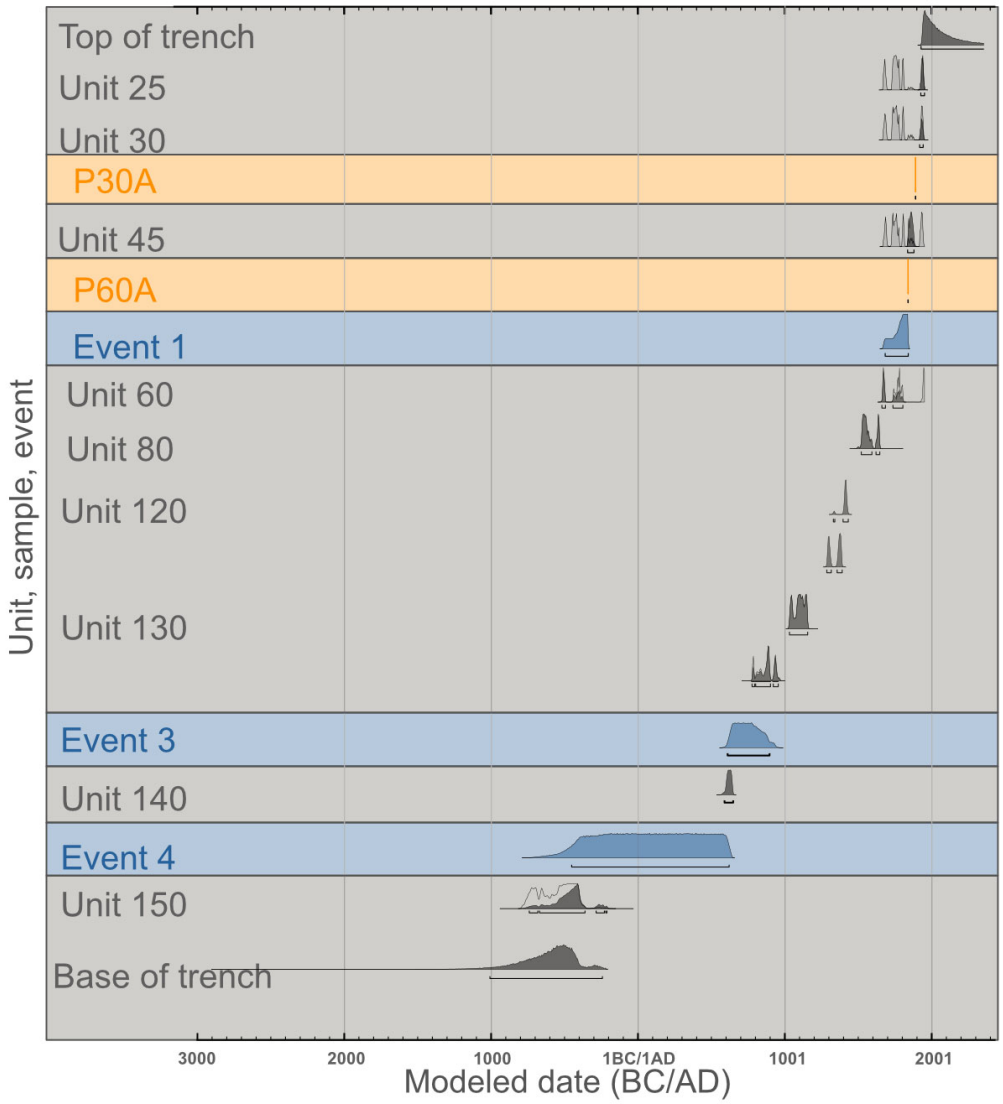

Fig. S3.

Modeled age of radiocarbon samples and events based on charcoal and invasive pollen species samples produced using OxCal software (Ramsey, 2009). Radiocarbon ages calibrated with the IntCal09 calibration curve (Reimer et al. 2013). The event ages are based on the ages of units above and below the event horizon. Darker probability density function (PDF) shading indicates trimming of age ranges based on stratigraphic constraints. Table 2 lists the radiocarbon samples with their respective carbon content and ages, following stratigraphic order.

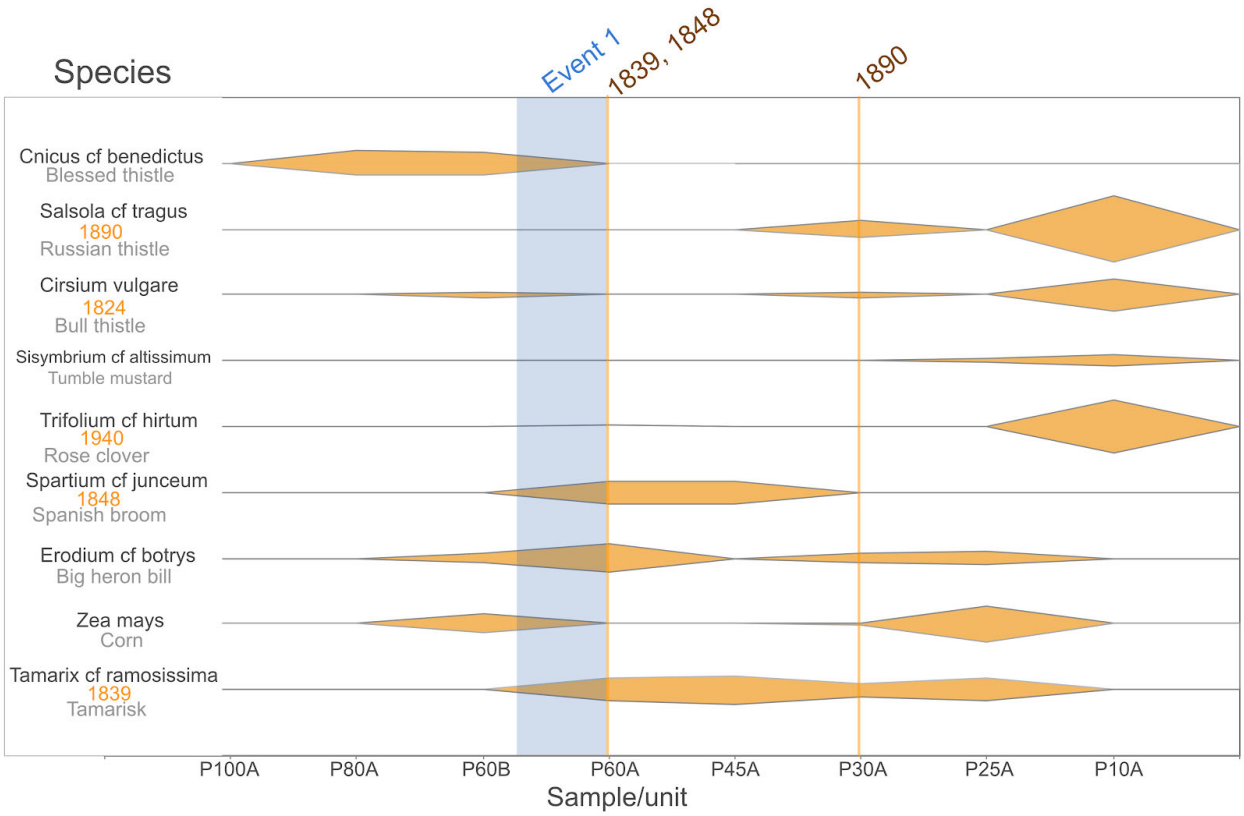

Fig. S4.

The kite diagram plots the appearance of pollen of plants introduced to California as a percentage. The percentage of introduced species has been calculated from the total pollen, including native species, found in the sample and taken as 100%. Only nine species out of twenty-three found were selected for the diagram as the most representative. The complete data are presented in Table 1. The X-axis represents sampling sites according to their order in the stratigraphic section and does not necessarily coincide with the timeline.

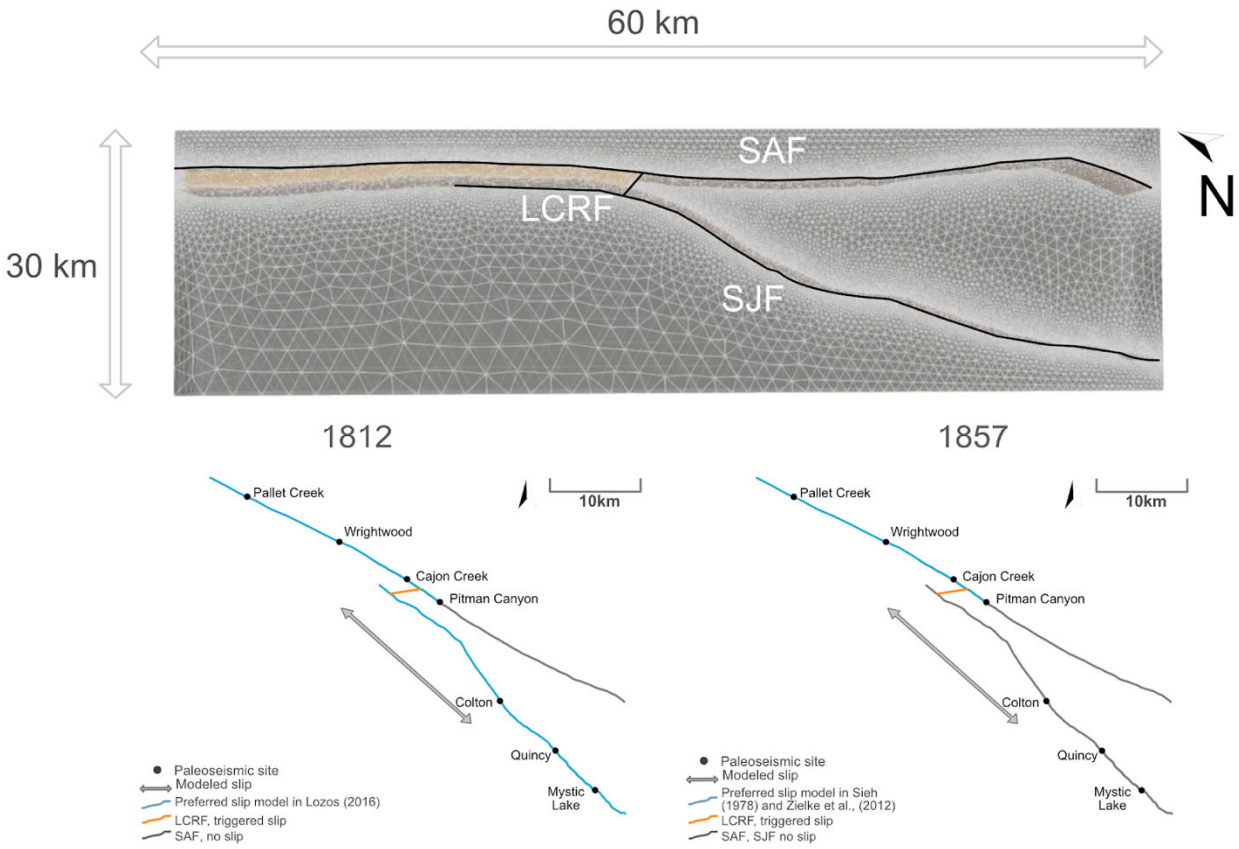

Fig. S5.

Top: Finite element mesh reproducing fault geometries in the Cajon Pass area. The San Andreas and the San Jacinto faults are based on the SCEC Community Fault Model's tsurfs. The geometry of the LCRF is a planar approximation projected from strike and dip measurements collected in the field. Bottom left: Slip model setup for the 1812 earthquake. Bottom right: Slip model setup for the 1857 earthquake.

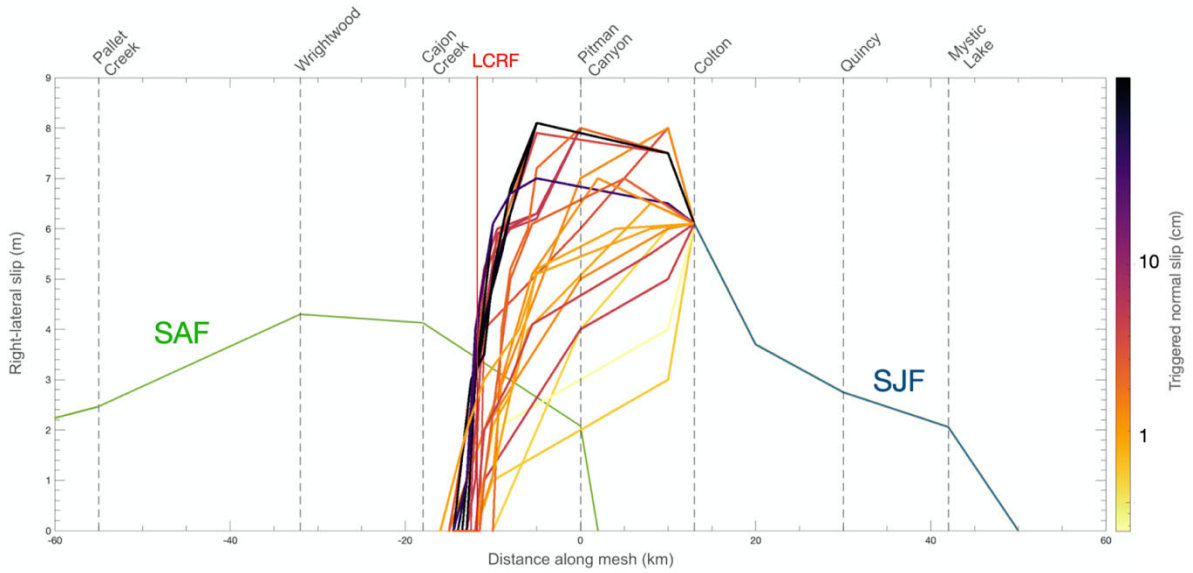

Fig. S6.

Slip models for the 1812 events through Cajon Pass. The grey and green line are right-lateral slip imposed on the SJF and the SAF based on the final slip in the preferred model in Lozos (2016). We test a suite of slip distributions on the SJF north of Colton. The lines associated with these slip distributions are color-coded by the normal slip those distributions trigger on the LCRF.

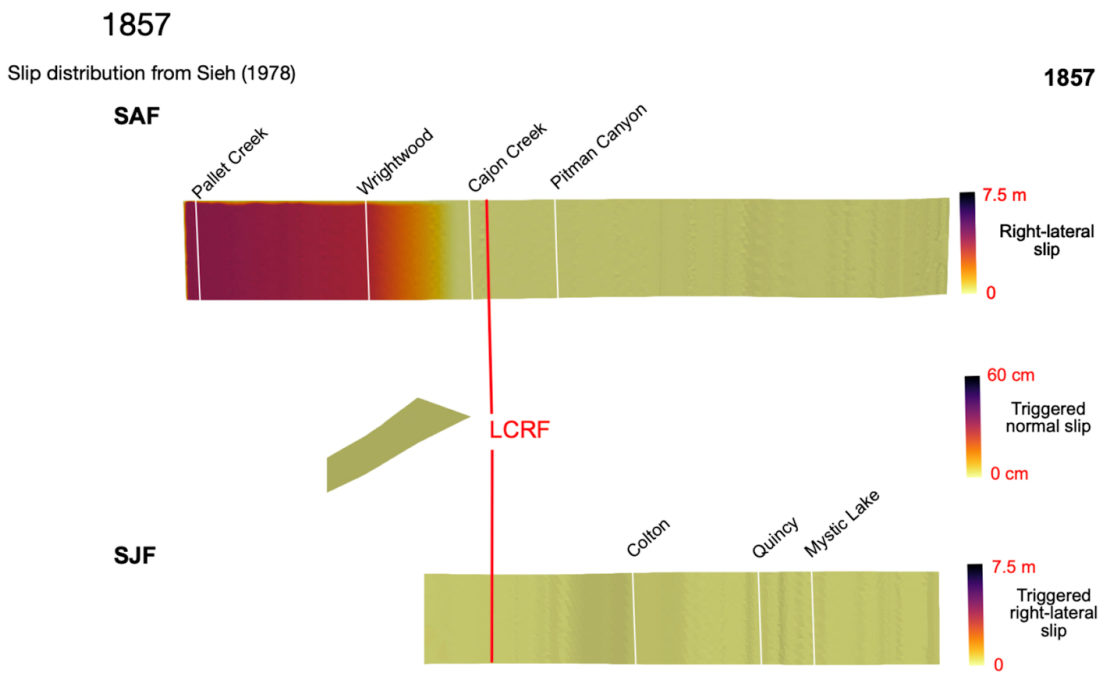

Fig. S7.

Top: Model for the 1857 event based on the slip distributions in Sieh (1978).

Table S1.

Table 1 is attached as an excel document. Raw and relative pollen data of non-native plant species present in soil samples from the LCRF. Table represents only introduced species; the rest of the counted pollen was not identified specifically and was listed as “varia”. Overall, these pollen grains were represented primarily by species of Fabaceae, Cyperaceae, Rosaceae, Rhamnaceae, Poaceae families. Tree pollen included some spp. of Quercus, Ulmus, Juglans, Abies and Sequoia sempervirens. All introduced species were checked for the time of their introduction to California. Species without exact dating are left blank. Pollen concentration was calculated for each sample and provides a proxy date of the relative plant coverage at the time of formation of the sediments.

Table S2.

Table 2 is attached as an excel document. Table 2 contains all of the radiocarbon samples with their respective carbon content and ages, following stratigraphic order.

Table S3.

Parameter	Value
Density crust	From SCEC CVM-S
Vs	From SCEC CVM-S
Vp	From SCEC CVM-S
Static friction coefficient (LCRF)	0.4
Cohesion (LCRF)	0 MPa
Element size	~100 m (near field) ~1000 m (far field)

Parameters used in the finite element models of the 1812 and 1857 events.